The kinetics of tweed-pattern formation in CuNiFe



1994 J. Phys.: Condens. Matter 6 1627

(http://iopscience.iop.org/0953-8984/6/9/005)

J. Phys.: Condens. Matter 6 (1994) 1627–1636. Printed in the UK

# The kinetics of tweed-pattern formation in CuNiFe

O Lyon† and J P Simon‡

† Laboratoire pour l'Utilisation du Rayonnement Electromagnétique, CNRS, Bâtiment 209D, 91405 Orsay Cédex, France

‡ Laboratoire de Thermodynamique et Physico-Chimie Métallurgiques, CNRS et INPG, BP 75, 38402 Saint Martin d'Hères Cédex, France

Received 18 October 1993

**Abstract.** The morphology of the tweed pattern during phase separation of CuNiFe single crystals has been followed by two-dimensional small-angle scattering (2D SAS), taking advantage of the x-ray constant enhancement by anomalous scattering. The 2D $[100]^*$ intensity maps have maxima with a fourfold symmetry and can be quantitatively described by three families of independent rows of (100) platelets alternatively enriched in Cu and in NiFe. Three length scales are defined: the mean platelet thickness $\lambda/2$ along the pile-up, its thickness distribution $\delta\lambda$, and its diameter $D$. Their kinetics are $\lambda \propto \tau^{-0.2}$, $\delta\lambda \propto t^{-0.27}$, and $D \propto t^{-0.4}$ respectively. These three length scales are thus independent: in this tweed-pattern coarsening, there is no global scaling due to the increase of the anisotropy and to the increase of the regularity in the pile-up.

## 1. Introduction

Age-hardenable alloys are constituted of a strengthening phase imbedded in a matrix. The size scale, and also the morphology, of this two-phase pattern is of principal importance for applications; if early stages of nucleation or of spinodal decomposition are of importance for the kinetics and the homogeneity of the particle sizes, the morphology of the pattern—i.e. the shape, imbrication etc—is more related to the coarsening process. This stage is generally described by the reduction of the surface tension obtained by evaporation–condensation, but very different patterns have been observed, such as bipercolated (in Fe Cr-based alloys), isolated spherical or cubic particles (in AlLi, or in superalloys), or tweed patterns (in NiTi, CuNiFe etc). The kinetics is always described by a power law $t^{-n}$ with small power ($0.05 < n < 0.4$), and authors generally describe the kinetics using single length scale, which implies that the pattern during coarsening is self-similar. Their approach is influenced by the basic model of Lifschitz and Slyozov (1961), which considers isolates spherical particles in a mean-field medium. On the other hand, elastic forces (Wang *et al* 1993) have been introduced to account for the anisotropy development and several snapshot of computed patterns have been given. Nevertheless there are few quantitative experimental studies of the evolution of the anisotropy.

The aim of this paper is to follow quantitatively the formation of the tweed pattern—i.e. the evolution of its anisotropy—by small-angle scattering (SAS) experiments on CuNiFe monocrystalline samples. This tweed pattern has been observed by transmission electron microscopy (Livak and Thomas 1971, Wahi and Stajer 1984) and by field ion imaging (Lopez *et al* 1993). It can be described by three families of platelets lying in the {100} planes in pile-up along [100] directions. The authors focus their interest on the mean

0953-8984/94/091627+10$19.50  

periodicity $\lambda$ along the pile-up, and isothermal kinetics are determined. On the other hand, CuNiFe is considered as a model system for phase separation and in a first approximation an isomorphic substitution of Ni and Fe was assumed: the SAS spectra (of neutrons) in polycrystalline samples (Wagner *et al* 1984) was compared to theoretical profiles deduced from models of phase separation of binary systems. A study by x-rays (Lyon and Simon 1988, called hereafter paper I), taking advantage of the anomalous scattering (ASAXS, i.e. the change of the atomic scattering factor of Fe or Ni near their K absorption edge) showed that there was indeed a partitioning between Cu on one side and Ni–Fe on the other, but that there was a supplementary segregation between Ni and Fe. Since this effect was suspected to be related to the anisotropy of the tweed pattern, the three-dimensional (3D) map of ASAXS was recorded on a monocrystalline sample of $Cu_{0.44}Ni_{0.42}Fe_{0.14}$ aged for 4 h at 550 °C (Lyon and Simon 1992, paper II): it consists of rather sharp maxima along the direction [100]* of the reciprocal space (figure 1); no secondary maxima were detected. The extraction of partial structure factors in symmetry directions showed that the supplementary Ni/Fe partitioning only affects the [100] directions and has about the same periodicity as the [100] Cu/NiFe pile-up. The intensity map can be reconstructed neglecting the correlations between the three families and between different rows of plates; the periodicity was deducted from the position of the maximum $q_{m100}$ along [100]*, and the diameter from the profile along MY of figure 1, which fits the structure factor $(\sin(qR)^2/(qR)^2)$ of a single platelet.

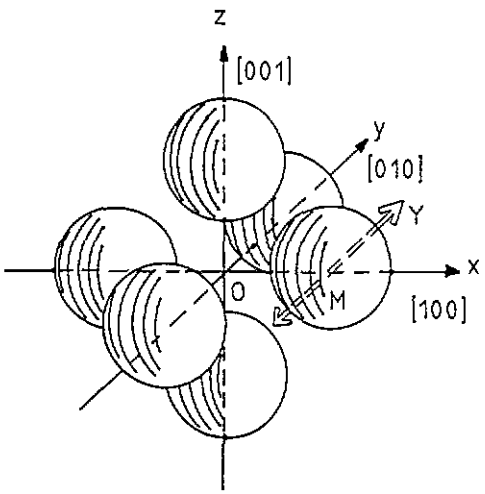


**Figure 1.** Schematic diagram of the 3D scattering pattern of a single crystal of CuNiFe aged for several hours at 550 °C. The spheres represent the maxima and simulate the half height isointensity surface.

The isothermal evolution of the anisotropy of the tweed pattern, followed by x-ray anomalous SAS on monocrystalline samples, is reported and discussed hereafter.

## 2. Experimental conditions

A $Cu_{0.44}Ni_{0.42}Fe_{14}$ single crystal has been grown up by the Bridgmann technique and homogenized. Slices were cut mechanically, and electrochemically thinned down to 0.015–0.025 mm in order to optimize their x-ray transmission. A second homogenization preceded

the water quench and finally samples were aged at 500 or 550 °C under high vacuum (further information is given in paper II).

ASAXS experiments were performed on beam line D22 of the synchrotron radiation facility of the Laboratoire d'Utilisation du Rayonnement Electromagnétique (LURE). After calibration of the double monochromator ($Ge_{111}$) by running absorption measurements through the Fe edge (7112 eV), the photon energy was fixed at 7104 eV. This energy is a good compromise between contrast (about twice than with a K$\alpha$ Co source) and degradation of the background (fluorescence, resonant Raman). The complete beam-line is under vacuum and a simple triple-axis sample holder was fitted to the sample changer.

The orientation of the sample was controlled by gas-filled 2D position-sensitive detector. However, since this detector has an insufficient spatial resolution, and an insufficient counting rate, image plates (IPs) were preferred. Their only difficulty for a quantitative exploitation of intensities lies in the natural de-excitation. In our case, neither the exposure time nor the delay between exposure and off-line reading of the IP can both be kept fixed. In order to make an internal calibration of the IP, we light an unused area of the IP by an $Fe^{55}$ source simultaneously with the scattering of the sample. Checks of this relative calibration were made and the overall precision is better than 1%.

The 2D scattering maps were corrected to account for monitoring, for sample thickness and transmission, and for residual parasitic scattering. The intensity (expressed in electron$^2$/atom/steradian) was scaled by comparison with the absolute calibration performed in a previous acquisition with the linear detector of the sample aged for 4 h at 550 °C.

## 3. Experimental results

The formation of the tweed pattern was followed by recording 2D intensity maps of the 001* zone axis. The as-quenched pattern is featureless, which shows that if any unmixing has started during the quench, its amplitude is below our detection sensitivity. The scattering pattern after 0.5 h at 500 °C presents a well defined intensity maximum, characteristic of phase separation, and this ring is isotropic. Anisotropy is already present after 3 h at 500 °C (figure 2); figure 2 also shows other typical 2D maps for further ageing conditions: it consists in all cases of fourfold symmetry so we can refer to the schematic representation of figure 1. 1D sections of these intensity maps are given in figures 3, 4, and 5 for the directions [100]*—i.e. OX of figure 1, [100]*, and [100]/[0$q_m$0]—i.e. MY of figure 1—respectively.

For short ageing times, the 100* humps are elongated along the direction MY tangential to the scattering ring. Their width along MY narrows more rapidly than their width along OX so, after 16 h at 550 °C, they are almost circular and the 2D iso-intensity map is constituted of four families of circles centred on a square. The representation of figure 1 is then almost exact for long ageing. The position of the saddle point along [110]* is then such that $q_{m110}/q_{m100} = 0.707$ (table 1), while a higher value for this $q_{m110}/q_{m100}$ ratio (table 1) is observed for shorter ageing times due to the stretching of the hump along MY. A supplementary feature appears for long ageing: the anisotropy strengthens along OX so that extra maxima are clearly visible after 66 h at 550 °C (figures 2 and 3) (they are already present after 16 h at 550 °C, but only as a shoulder); they can be indexed as 300* if we index the dominant maxima as 100*. The 200* order is clearly absent. From the iso-intensity maps we can also deduce maxima on the 210* positions after 16 and 66 h at 550 °C.

To quantify the kinetics of the 100* maxima, we measure its position $q_{m100}$, its FWHM $\Delta q_{OX}$ and $\Delta q_{OY}$ along OX and along MY, respectively, and its intensity $I_m$ (figure 6):

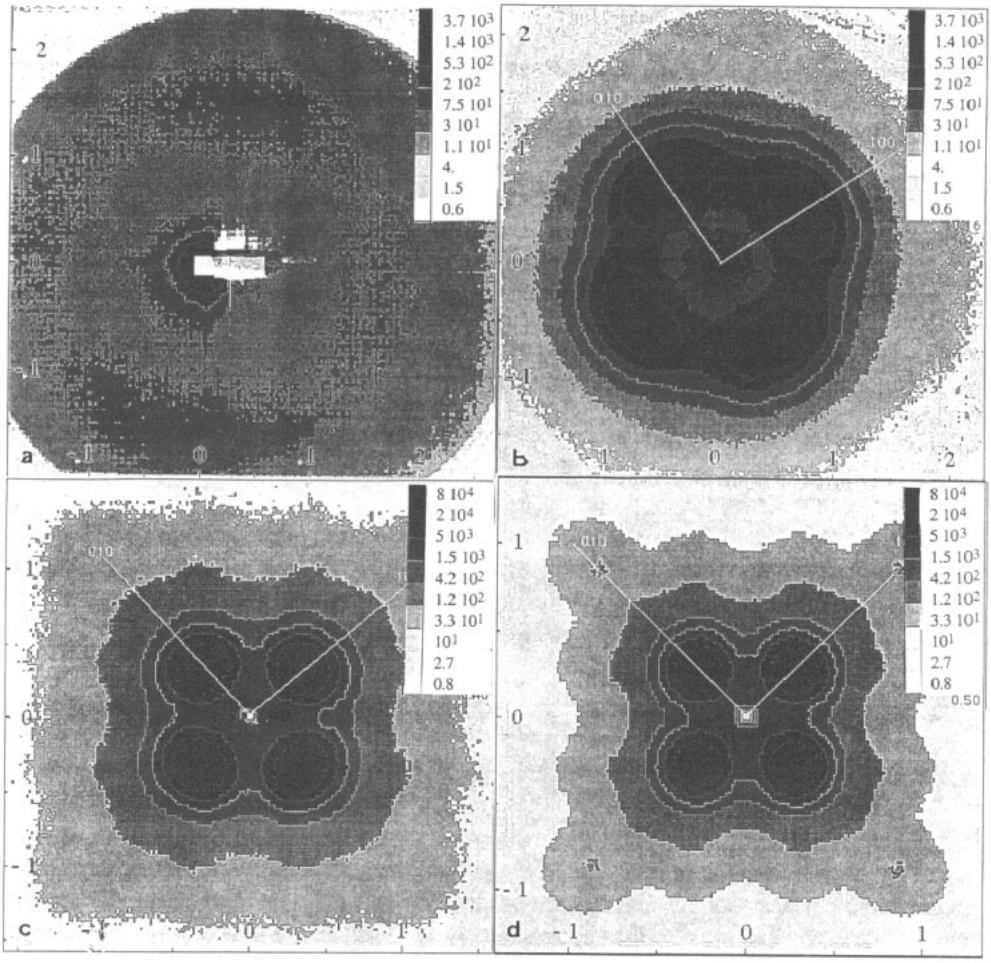


**Figure 2.** Isointensity maps of a monocrystalline $Cu_{0.44}Ni_{0.42}Fe_{0.14}$ sample in the 001* zone axis for different ageing conditions: (*a*) 3 h at 500 °C, (*b–d*) 1.07, 16, and 66 h at 550 °C.

they can be analysed as power laws at 500 °C, as usual for isothermal kinetics of phase separation:

$$\begin{aligned} q_{m100} &\propto t^{a} \qquad a = -0.19 \\ \Delta q_{OX} &\propto t^{b} \qquad b = -0.25 \\ \Delta q_{MY} &\propto t^{c} \qquad c = -0.36 \\ I_{m} &\propto t^{d} \qquad d = 0.83. \end{aligned} \tag{1}$$

Let us notice that the position of the maximum in polycrystalline samples is almost equal to $q_{m100}$: for short ageing times, $q_m$ weakly depends on the direction, while for late times, the intensity is so concentrated along the [100]* directions that these directions impose their characteristics on the powder-like scattering profile.

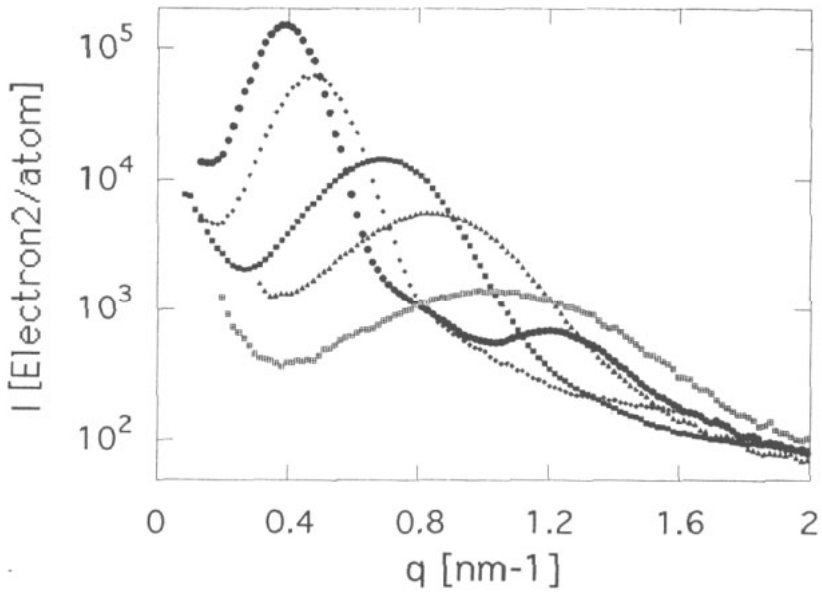


**Figure 3.** Kinetics of the scattering profiles along a {100}* direction: ⊞, 3 h at 500 °C; ▲, 1.07 h at 550 °C; ■, 4 h at 550 °C; ♦, 16 h at 550 °C; ●, 66 h at 550 °C.

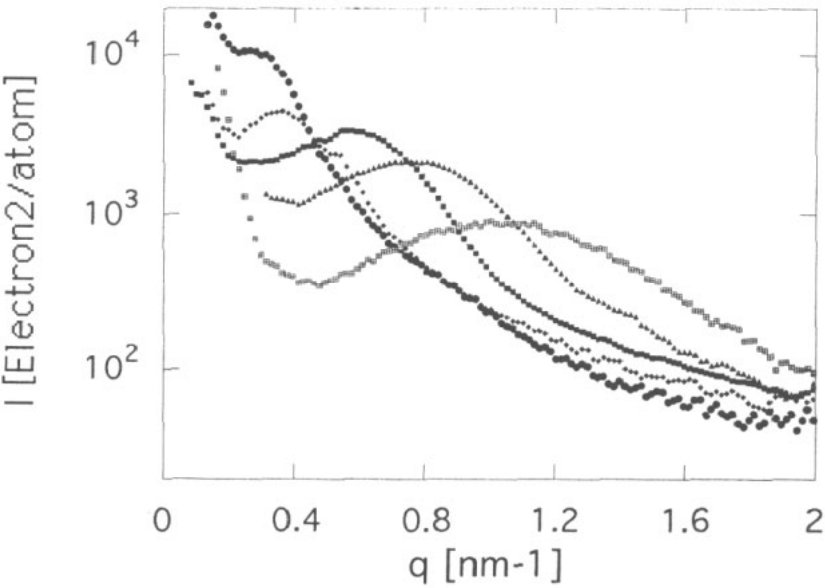


**Figure 4.** Kinetics of the scattering profiles along a {110}* direction; same notations as figure 3.

If we go further with the comparison of $q_m$ with polycrystals, it has been shown (Wagner *et al* 1984, Lyon and Simon 1988) that the $q_m$ kinetics between 460 and 550 °C were the same when a time scaling factor was included:

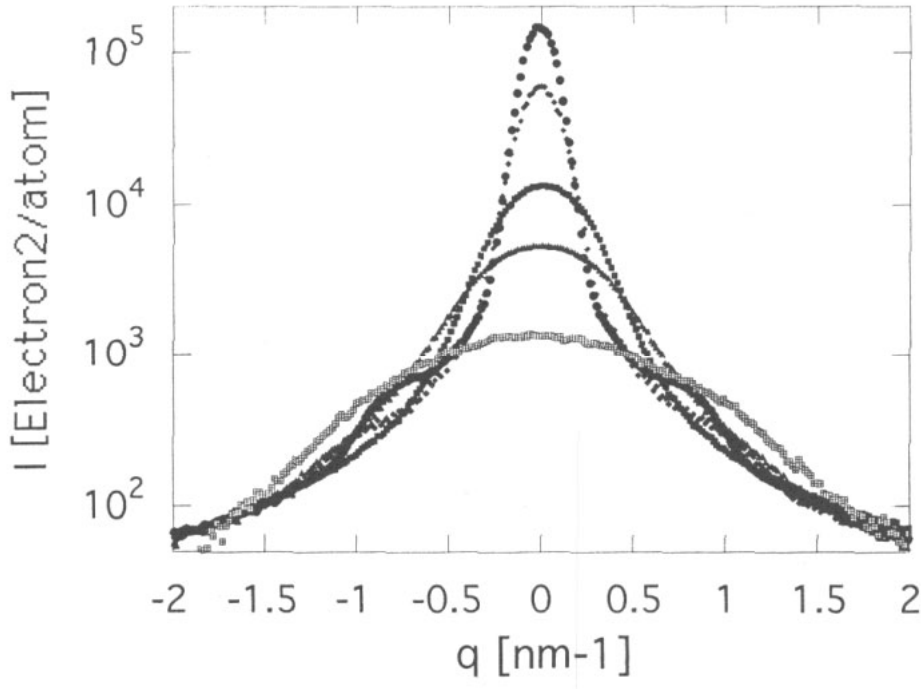


**Figure 5.** Kinetics of the scattering profiles along a direction perpendicular to a [100]* direction and centred on the maximum (direction MY of figure 1); same notations as figure 3.

**Table 1.** Kinetics of the tweed-pattern formation

| | Equivalent time at 550 °C (h) | | | | | |
|---|---|---|---|---|---|---|
| | 0.056 (0.5 h/500 °C) | 0.336 (3 h/500 °C) | 1.07 | 4 | 16 | 66 |
| $\lambda$ (nm) | 4.05 | 6.4 | 7.6 | 9.2 | 13.4 | 16 |
| $\lambda$ (TEM; Wahi and Stajer 1984) | — | $4.0 \pm 0.5$ | $6.0 \pm 0.5$ | $9.0 \pm 1$ | $11 \pm 1$ | $16 \pm 1$ |
| $D$ (nm) | — | 3.65 | 6.9 | 10 | 21 | 27.7 |
| $q_{m110}/q_{m100}$ | — | 0.99 | 0.92 | 0.84 | 0.71 | 0.68 |
| $I_{m110}/I_{m100}$ | — | 0.61 | 0.4 | 0.2 | 0.08 | 0.08 |
| $I_m \Delta q_{OM} \Delta q_{MY}^2$ | — | 2.87 | 1.84 | 1.7 | 0.94 | 1.15 |

$$t_s(T^*) = t(T) \exp[(Q/k_B)(1/T^* - 1/T)]$$

where $t_s$ is the time equivalent at a reference temperature $T^*$ to the experimental ageing time $t(T)$ and $Q$ is the interdiffusion activation energy ($Q = 2.4$ eV). The use of 0.5 and 3 h at 500 °C together with data at 550 °C gives essentially the same results:

$$q_{m100} \quad \propto t^a \quad a = -0.19$$

$$\Delta q_{OX} \quad \propto t^b \quad b = -0.235$$

$$\Delta q_{MY} \quad \propto t^c \quad c = -0.4.$$

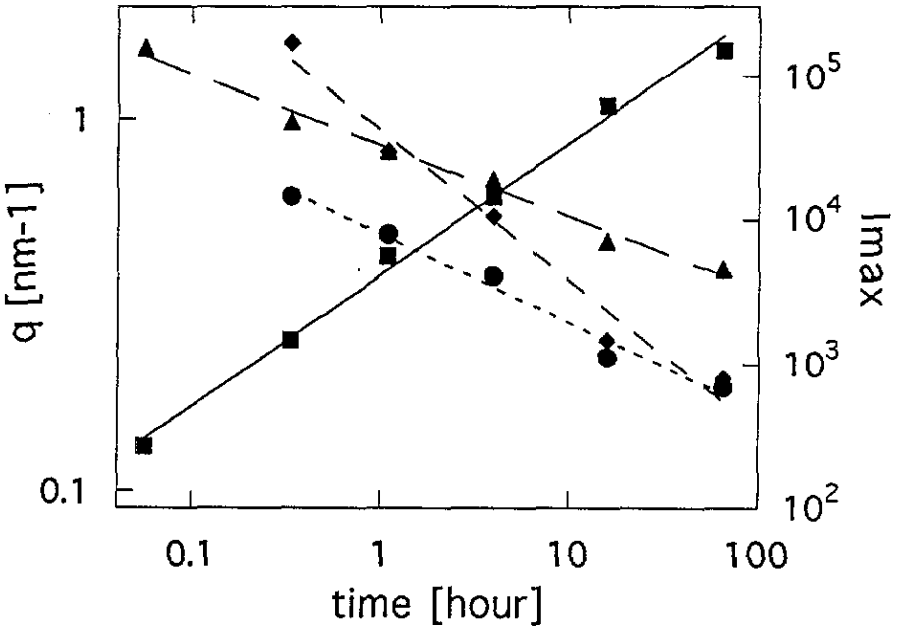


**Figure 6.** Power-law fits of the characteristic parameters: ▲, $\Delta q_{m100}$; ♦, $\Delta q_{OX}$; ●, $\Delta q_{MY}$; ■, $I_m$.

## 4. Discussion

Following paper I we have modelled the tweed pattern by three families of discs lying on the {100} planes. They are stacked in rows along ⟨100⟩ directions and we neglect the correlations between rows and families. This is consistent with the sharp maximum along 100* and with a scattering profile along MY of the form $[\sin(qR)/(qR)]^2$. Table 1 gives the length scales of the tweed pattern: the pseudoperiodicity $\lambda$ along ⟨100⟩ is given by $2\pi/q_m$ and the diameter of the platelets by $D = 2R$. Since our alloy is situated at the centre of the miscibility gap, both phases have almost the same volume fraction: the thickness of an individual platelet is $\lambda/2$.

The $\lambda$ values are in agreement with a TEM study (Wahi and Stajer 1984) (table 1). On the other hand, the $\lambda$ evaluation made previously using polycrystalline samples and the averaging formula $2\pi/1.3q_m$ (Wagner *et al* 1984) was inexact: the factor of 1.3 originated from an averaging of the $\lambda$ values in all directions but, as shown in the last paragraph of section 2, off-oriented crystals of a polycrystalline sample contribute weakly to the total intensity, so that $q_{m\ poly} \simeq q_{m100}$.

The diameter of the platelets increases more rapidly than $\lambda$, so that the aspect ratio $2D/\lambda$ increases from 1.3 to 4 in the studied range and reaches several tenths in TEM observations of overaged samples (Livak and Thomas 1971). Therefore this is not an equilibrium shape due to an anisotropy of interfacial tension but a growth morphology. The growth of the edges is much more rapid than the thickening but this does not mean that the ledge mechanism describing the growth of intermetallic precipitates should automatically apply to the present case of phase separation. On the other hand, almost flat 100 interfaces as well as the

screening of the diffusion field by the row of platelets make a Lifschitz–Slyozov mechanism totally unadapted: the diffusion fields are local. The second direction of interpretation is the reduction of the coherency energy, the pile-up aligning along the elastically soft [100] directions of Cu and of NiFe. The simulations of Wang and co-workers (1993), including the elastic energy term, qualitatively reproduce the patterns, either bipercolated (no strain energy) or tweed pattern.

The regularity of the pile-up in the row can be qualitatively determined through the relative FWHM along $(100)^*(\Delta q_{OX}/q_{m100})$: this decreases from 0.87 to 0.5. These values cannot be analysed in a crystallographic way since this would mean a correlation distance along the row smaller than two periods. Moreover the OX scattering profile is not symmetric as it would appear for a block effect. The other interpretation is fluctuations of thicknesses of platelets in the row: the decrease of the relative FWHM indicates a narrowing of the thickness distribution. This interpretation is consistent with the appearance of higher orders, the reason why the third order emerges instead of the second harmonics being the well known annulation of the 1D structure factor when both domains have the same thickness. The existence of the $210^*$ is more puzzling: our approximation of independent families is too coarse. Indeed some field ion images (figure 2 of the article by Lopez *et al* (1993) for instance) suggest that two families may be locally attached by the edges, forming a herring-bone pattern.

Another pertinent parameter of phase separation is the integrated intensity:

$$\hat{I} = \iiint I(q)\,\mathrm{d}q = f_v(1 - f_v)\Delta\rho^2$$

where the integration extends over the first Brillouin zone, where $f_v$ is the second-phase volume fraction and $\Delta\rho$ the electronic contrast between the two phases. In the coarsening regime, the compositions and volume fractions are almost equal to the equilibrium values, so a constant integrated intensity is a good indication that this regime has been reached.

In polycrystalline samples $I(q)$ is now isotropic so that the integrated intensity simplifies to

$$\hat{I} = 4\pi \int I(q)q^2\,\mathrm{d}q$$

where $q$ is the wavenumber of the wavevector $q$.

In our previous study of polycrystalline samples of the same composition for similar ageing conditions $\hat{I}$ was found to be fairly constant at a given temperature and the absolute $\hat{I}$ value was of the order of magnitude expected from the miscibility gap. The $\hat{I}$ evaluation in the present case would require more complete measurements than the $001^*$ intensity maps. Nevertheless, since the intensity is concentrated in the $001^*$ peaks, a rough estimation would be

$$\hat{I} \propto \Delta q_{OX}\Delta q_{MY}^2 I_m.$$

Values are rather scattered, decreasing at longer times. Similarly the power-law coefficients of equations (1) should obey the following relationship:

$$b + 2c + d \simeq 0$$

which is not followed.

Another check of coarsening is the classical rescaled scattering factor $I(q)/I_m$ versus $q/q_m$ (Fratzl and Lebowitz 1989), which fits a profile independent of ageing in the case of a single pertinent length scale. This is almost always observed for polycrystalline profiles and has been taken as a signature of coarsening. In the present case, the diameter of platelets of course scales since the scattering profile along MY is a $[\sin(qR)/(qR)]^2$ law. In contrast, the scaling is not obeyed in the pile-up direction as evidenced by figure 7: the thickening of platelets is accompanied by a narrowing of the size distribution. There are two independent parameters in the direction of the pile-up. Finally since the shape ratio $2D/\lambda$ increases with time, the description of the tweed pattern by three independent length scales $(D, \lambda, \delta\lambda)$ is justified.

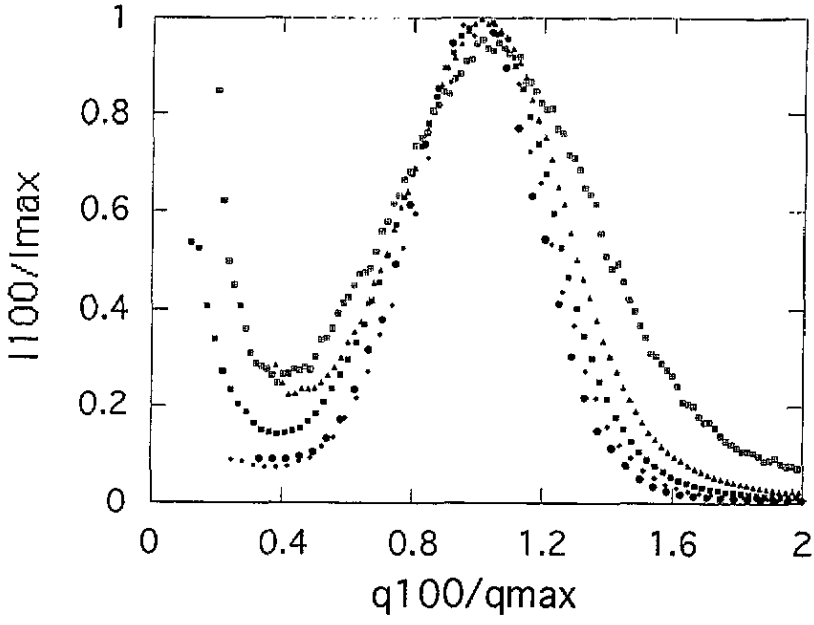


**Figure 7.** Scaling of the scattering profile along the 100* direction: same notations as figure 3.

The present results are at first glance in contradiction with the previous scaling obeyed in polycrystalline samples. Since these scaled profiles are found to be independent of the pattern (bipercolated or tweed pattern for FeCr or CuNiFe (Bley *et al* 1993)), it seems that the powder-like averaging rubs out the characteristics of the pattern: the length scale and kinetics thus obtained are apparent and hide a more complex phenomenon: it appears that scaling is not a sensitive test of the late stages of phase separation.

As a conclusion this modelling of coarsening during tweed pattern formation in CuNiFe with three independent length scales $\lambda$, $\delta\lambda$, and $D$ appears to be an intermediate step towards a full description of the tweed pattern.

## References

Bley F, Desplats J, Guyot P, Livet F, Mainville J and Simon J P 1993 *J. Physique Coll.*
Fratzl P and Lebowitz J L 1989 *Acta Metall.* 37 3245

Lifschitz I M and Slyozov V V 1961 *J. Phys. Chem. Solids* **19** 35
Livak R J and Thomas G 1971 *Acta Metall.* **19** 497
Lopez V M H, Sano N, Sakurai T and Hirano K 1993 *Acta Metall.* **41** 265
Lyon O and Simon J P 1988 *J. Phys. F: Met. Phys.* **18** 1787
—— 1992 *J. Phys.: Condens. Matter* **4** 6073
Wagner W, Poerschke R and Wollenberger H 1984 *Decomposition of Alloys: the Early States* ed P Haasen *et al* (Oxford: Pergamon) p 170
Wahi R P and Stajer J 1984 *Decomposition of Alloys: the Early States* ed P Hassen *et al* (Oxford: Pergamon) p 165
Wang Y, Chen L Q and Katchaturian A G 1993 *Acta Metall.* **41** 270